Topological phase transitions and Berry-phase hysteresis in exchange-coupled nanomagnets

Ahsan Ullah [ORCID],[*] Xin Li, Yunlong Jin, Rabindra Pahari, Lanping Yue, Xiaoshan Xu,
Balamurugan Balasubramanian, David J. Sellmyer,[†] and Ralph Skomski[†]

Department of Physics & Astronomy and Nebraska Center for Materials and Nanoscience, University of Nebraska, Lincoln, NE 68588

Topological phase in magnetic materials yields a quantized contribution to the Hall effect known as the topological Hall effect, which is often caused by skyrmions, with each skyrmion creating a magnetic flux quantum $\pm h/e$. The control and understanding of topological properties in nanostructured materials is the subject of immense interest for both fundamental science and technological applications, especially in spintronics. In this work, the electron-transport properties and spin structure of exchange-coupled cobalt nanoparticles with an average particle size of 13.7 nm are studied experimentally and theoretically. Magnetic and Hall-effect measurements identify topological phase transitions in the exchange-coupled cobalt nanoparticles and were used to discover a qualitatively new type of hysteresis in the topological Hall effect—namely, Berry-phase hysteresis. Micromagnetic simulations reveal the origin of the topological Hall effect—namely, the chiral domains, with domain-wall chirality quantified by an integer skyrmion number. These spin structures are different from the skyrmions formed due to Dzyaloshinskii–Moriya interactions in B20 crystals and multilayered thin films, and caused by cooperative magnetization reversal in the exchange-coupled cobalt nanoparticles. An analytical model is developed to explain the underlying physics of Berry-phase hysteresis, which is strikingly different from the iconic magnetic hysteresis and constitutes one aspect of 21st-century reshaping of our view on nature at the borderline of physics, chemistry, mathematics, and materials science.

I. INTRODUCTION

Topological phase transitions (TPTs) permeate areas such as superfluid and superconductors [1,2], basic quantum mechanics [3,4], fractional quantum Hall effects [5], and topological insulators [6], and therefore have gained significant interest in both science and technology. TPTs are very different from ordinary Landau-type phase transitions [4,7–9]. Rather than involving symmetry breaking and order-parameter changes, they are characterized by changes in topological numbers. For example, coffee cups have one hole, located in the handle, and are therefore characterized by the topological number (Euler genus) $g = 1$. A flat pancake has no holes ($g = 0$), so that the piercing of a number of holes into a pancake is a trivial example of a TPT.

Topological phase transition is in contrast to magnetic hysteresis, which is based on a phase transition between an ordered low temperature and a disordered high temperature [1–6,10–12]. An intriguing aspect of magnetic hysteresis is its relation to magnetic phase transitions. Figures 1(a) and 1(b) compares the atomic-scale origin of ferromagnetism with the nanoscale or "micromagnetic" origin of hysteresis. When a ferromagnet is cooled below the Curie temperature T_c, it develops a spontaneous magnetization M_s [Fig. 1(a)]. This process is a Landau-type phase transition, defined as a singular change of a local-order parameter (M) due to spontaneous

symmetry breaking. The ordered phase has the character of a $k = 0$ Goldstone mode, which has a magnetization that can point in any direction [Fig. 1(a)]. This degeneracy is removed by symmetry-*violating* terms in the Hamiltonian, such as magnetic anisotropy [13].

Magnetic hysteresis, Fig. 1(b), is on top of the Landau transition [Fig. 1(a)]. When a magnetic material is subjected to an external field H, then its magnetization $M(H)$ is generally not single-valued, but splits into ascending and descending branches. A well-known example is small nanoparticles of volume V and anisotropy energy $K_1 V \sin^2\theta$ in a magnetic field $H = H_z$. The color coding throughout this article is $M_z(\mathbf{r}) = +M_s$ (red), $M_z(\mathbf{r}) = -M_s$ (blue), and intermediate (yellow). For positive K_1, $\theta = 0$ (red) and $\theta = 180°$ (blue) are energetically favorable, but separated by an energy barrier $K_1 V (\theta = 90°)$. This energy barrier needs some external field to be overcome and is therefore the reason for the hysteresis.

While topology has a long history, the idea of topological phase transition goes back to the Lifshitz transition [4,7]. Figure 1(c) shows the k-space meaning of the Lifshitz transition in metals. Itinerant electrons fill the available electron states until the Fermi level is reached. The occupancy at the Fermi level (gray) depends on the number of electrons, and there are several scenarios that change the topological quantum number Q, such as external mechanical pressure and chemical addition of electrons. Each Fermi-surface region (gray) yields an integer contribution to Q, regardless of the size and shape of the pocket. Topological concepts are now applied to many areas of physics, from skyrmions [7,8,15–20]
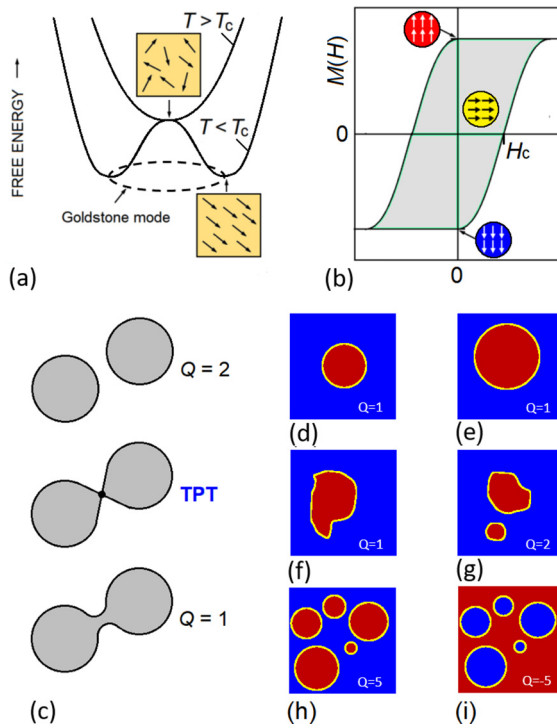
*aullah@huskers.unl.edu
†Deceased.

FIG. 1. Phase transitions: (a) Curie transition (magnetic Landau transition), (b) magnetic hysteresis, (c) Lifshitz transition in metal, and (d–i) topological phase transitions in a magnetic thin film with perpendicular anisotropy. In (c), the gray areas denote the k-space region occupied by electrons at the Fermi level. In (d–i), red and blue regions indicate positive (↑) and negative (↓) magnetizations with respect to the film plane. Topological phase transitions are characterized by topological numbers Q. The topological protection in the micromagnetic case is experimentally established—for example, through the "blowing" of skyrmions [14–16].

to topological insulators and other quantum materials [21–30], all of them fascinating research topics in their own rights.

Figures 1(d)–1(i) shows the magnetic analog of the Lifshitz transition in a thin film. The field H is perpendicular to the film and affects ↑ (red) and ↓ (blue) regions separated by domain walls (yellow). The underlying micromagnetism is very similar to that of magnetic skyrmions [31–36] and to XY-model transitions [8]. When an electrical current flows through the film, then the spins of the conduction electrons exchange interact with the local magnetization $M(r)$ and become, in general, noncoplanar noncollinear. This noncollinearity creates a Berry curvature [5], an emergent magnetic field, and subsequently a Hall-effect contribution known as the topological Hall effect (THE) [5,33]. These effects are proportional to the *skyrmion density* [31,33,37,38],

$$\Phi = \frac{1}{4\pi} \boldsymbol{m} \cdot \left(\frac{\partial \boldsymbol{m}}{\partial x} \times \frac{\partial \boldsymbol{m}}{\partial y} \right), \qquad (1)$$

where $\boldsymbol{m} = \boldsymbol{M}(r)/M_s$ is the normalized magnetization and the xy-plane is the film plane. The emergent magnetic flux that corresponds to the THE is equal to $Q\,h/e$, where $Q = \int \Phi\, dx dy$ is the skyrmion number and h/e is the magnetic flux quantum. In granular thin films, such as the one considered here, there are also nonzero derivatives $\partial \boldsymbol{m}/\partial z$. By virtue

of measurement geometry, $\partial \boldsymbol{m}/\partial z$ does not contribute to the THE [33], but it is one source of noise [39]. The skyrmion density is nonzero for spins $\boldsymbol{m}(\mathbf{r})$ that are both noncollinear and noncoplanar, and Eq. (1) is actually a continuum version of the triple product or spin chirality $\chi_s = \boldsymbol{m}_i \cdot (\boldsymbol{m}_j \times \boldsymbol{m}_k)$, where $\boldsymbol{m}_i = \boldsymbol{m}(\boldsymbol{R}_i)$ describes the atomic spins that cause the conduction electrons to develop their Berry phase.

Much of the fascination with topological phase transitions originates from the great simplicity of the mathematics conveyed by Eq. (1), which is summarized in Supplemental Material SA [40]. In skyrmionic structures such as those of Figs. 1(d)–1(i), the spins inside the red and blue regions are parallel ($m = \pm e_z$), so that $\partial \boldsymbol{m}/\partial x$, $\partial \boldsymbol{m}/\partial y$, and Φ are zero. The integral over Φ therefore reduces to an integral over the yellow domain-boundary regions in Figs. 1(d)–1(i). It can be shown that

$$Q = \frac{1}{2\pi} \oint \boldsymbol{k}.d\boldsymbol{l}, \qquad (2)$$

where κ is the curvature of the region's yellow boundary, and the integral in Eq. (2) has the value 2π [41]. This integral is equal to ± 1 for any area enclosed by a single yellow boundary [41]. While Eq. (2) is valid for arbitrary domain shapes, it requires domain walls free of internal singularities such as Bloch lines [33,42]. Mathematically, $\boldsymbol{M}(r)$ is a fiber bundle [43] on the base space r and therefore is locally flat but globally nontrivial [44]. In fact, Figs. 1(d)–1(i) provides a simple example of a bulk-boundary equivalence, a feature that forms a cornerstone of topological physics [22]. The sign of Q depends on the vorticity [45] of the spin structure—that is, on whether the region enclosed by the yellow boundary is red ($Q = +1$) or blue ($Q = -1$). In particular, Q is independent of the clockwise or counterclockwise chirality of Bloch walls in the yellow region (Supplemental Material Figs. S1 and S2 [40]).

As discussed earlier, TPTs do not increase or decrease order parameters, but consist of changes in topological numbers. This leads to the question of whether such transitions lead to hysteretic features beyond magnetic hysteresis. This hysteresis was not recognized in earlier research, because available systems had micron-size features, rather than nanoscale feature sizes, which makes it very difficult to detect the Berry curvature in Hall-effect measurements. In this work, we have fabricated exchange-coupled cobalt nanoparticle films having a much smaller average size of about 13.7 nm, and show topological phase transitions and Berry phase hysteresis using experiments. The experimental results and the underlying physics are also explained using micromagnetic simulations and an analytical model.

II. EXPERIMENTAL AND COMPUTATIONAL METHODS

An inert gas condensation-type, cluster deposition method, schematically shown in Supplement Material Fig. S3(a) in Supplemental Material SB [40], is described elsewhere [46]. First, cobalt nanoparticles were produced by dc magnetron sputtering using a mixture of argon and helium with a power of 200 W in a gas aggregation chamber. After the formation, the nanoparticles were extracted toward the deposition chamber and deposited as a dense film on a silicon (100) substrate

having a Hall bar. The base pressure of the gas aggregation chamber was 6×10^{-8} Torr and the respective argon and helium flow rates were maintained at 400 and 100 SCCM (cubic centimeter per minute at STP), respectively. The pressure in the cluster formation chamber during the deposition was 0.7 Torr.

The cobalt nanoparticles were deposited with a low coverage density on a thin carbon film supported by copper grids for transmission electron microscopy measurements using an FEI Tecnai Osiris scanning transmission electron microscope. For magnetic and electron-transport measurements, the cluster-deposited nanoparticles were deposited for an extended time as a dense film, as discussed in our previous work [46,47]. The previous measurements were performed using a superconducting quantum interference device (SQUID) and physical property measurement system (PPMS), respectively. A schematic of a dense nanoparticle film is shown in Supplemental Material Fig S3(d) [40], and therefore they are exchange-coupled and conducting. The thickness of the cobalt nanoparticle film is about 270 nm. The conduction channels for the Hall contacts were fabricated before depositing the cobalt nanoparticles, as described in Ref. [46]. To prevent oxidation upon exposure to air, the cobalt nanoparticle film was capped with a SiO_2 layer of about a 10-nm thickness immediately after deposition, using radio frequency (RF) magnetron sputtering. The SiO_2 cap layer is thinner (about 10 nm) compared to the cobalt nanoparticle film (about 270 nm thick) and is also diamagnetic. Therefore, the film–SiO_2 interface is not expected to affect the magnetic and transport properties of the cobalt nanoparticle films. The particles have an average size of 13.7 nm with a narrow size distribution [see Supplemental Material Fig. S3(b) and S3(c) [40]] and crystallize in the hcp structure, as shown in Supplemental Material Fig. S4 [40]. A commercial atomic force microscope (AFM)/magnetic force microscope (MFM) (Atto AFM/MFM Ixs; Attocube Systems) was used to map the topography and magnetic images at 200 K. During the measurement, magnetic force microscopy was performed in constant height mode (single pass) with the PPP-MFMR tip from NANOSENSORS. The lift height is 250 nm and the scan speed is 5 μm/s.

To model the magnetic and Berry-phase hysteresis numerically, we have performed micromagnetic simulations using *ubermag* supported by OOMMF [48,49]. We have numerically extracted skyrmion number Q from the spin structure. A densely packed film of 1000 cobalt nanoparticles has been considered. The cobalt particles have sizes of about 13.7 nm, and the total size of the simulated system, shown in Supplemental Material Fig. S10 [40], is 240 nm×240 nm×60 nm. We have used a computational cell size of 1.8 nm, which is well below the exchange length l_{ex} [12]; a coherence radius of 5.099 l_{ex} of cobalt (10 nm) [12]; the domain-wall width (14 nm) of cobalt [12]; and the current particle size. This cell size ensures a reasonable real-space resolution of $M(r)$.

Aside from the numerical cell size, our continuum approach is valid on length scales much larger than the Co-Co interatomic distance of 0.25 nm. This makes it possible to consider the thin film as a fiber bundle $M(r)$ with the base space r, allowing us to define quantities such as the boundary curvature κ. A refined atomistic analysis, not considered here, would yield corrections due to the discrete nature of the atoms at the particle's surfaces and near contact points (see, e.g., Sec. 4.5 in Ref. [12]). In particular, the crystal structure of cobalt is inversion symmetric, so there are no bulk Dzyaloshinskii–Moriya interactions (DMIs). Corrections to the magnetization angles caused by the DMI of surface atoms are likely but probably very small. Note that the cobalt nanoparticles exhibit nanoscale inversion symmetry, as contrasted, for example, to the magnetism of Co/Pt bilayers [27].

The cluster deposition method yields isotropic nanoparticles with random grain orientation and therefore a random orientation of the easy magnetization axes n of the hcp cobalt particles, obeying $\langle n_x \rangle = \langle n_y \rangle = \langle n_z \rangle = 0$ and $\langle n^2 \rangle = 1$. This randomness in simulations, clearly visible in Supplemental Material Fig. S10(b) [40], was implemented by using Python np.random.uniform [49]. The particles touch each other, as shown in Supplemental Material Fig. S3(d) [40], so that the exchange stiffness A near the contact points is the same as in bulk cobalt.

Temperature-dependent micromagnetic effects are included in the lowest order—that is, by considering the intrinsic materials parameters M_s, K_1, and A as temperature dependent. This approach accounts for the atomic spin disorder outlined in Fig. 1(a). Other finite-temperature corrections—caused, for example, by magnetic viscosity [12]—have been ignored. In our simulations, we have taken values of $M_s = 1300$ kA/m, $K_1 = 0.58$ MJ/m^3, and $A = 10.3$ pJ/m [12].

III. RESULTS AND DISCUSSION

Transmission electron microscopy and the corresponding particle-size histogram show an average particle size of 13.7 nm with a standard deviation $\sigma/d \approx 0.15$ [Supplemental Material Fig. S3(b) and S3(c) [40]] for the cobalt nanoparticles. We have conducted magnetic, electron-transport, and Hall-effect measurements at temperatures from 10 K to 300 K for the dense cobalt nanoparticle films, as schematically shown in Supplemental Material Fig. S3(d) [40]. The magnetic hysteresis loops are shown in Supplemental Material Fig. S5 [40], and the measured coercivities are 0.18 T at 10 K and 0.04 T at 300 K.

Figure 2 compares the experimental data on a cobalt nanoparticle thin film [Fig. 2(a)] with numerical predictions [Fig. 2(b)]. The THE was extracted from Hall-effect measurements (Supplemental Material Fig. S6 [40]), as explained in Supplemental Material SB [40]. We see that the Berry-phase hysteresis loops (colored) look qualitatively different from the magnetic hysteresis loops (black), and that they are much broader than the magnetic ones. Figure 2(a) and 2(b) also shows that Berry-phase hysteresis loops contain more features than magnetic hysteresis loops. There are both mathematical and physical explanations for these differences. Mathematically, Eq. (1) contains derivatives, which amounts to a numerical amplification of details. Physically, Berry-phase hysteresis loops exhibit a more complicated dependence on the spin structure, because Φ is more complicated than m.
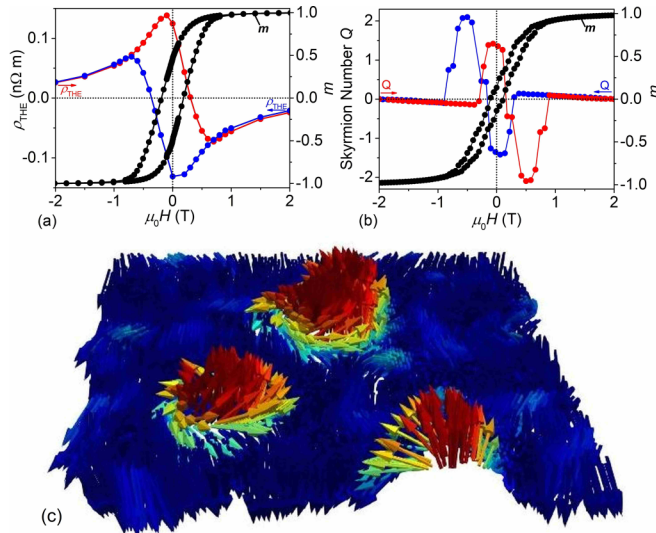
FIG. 2. Magnetic hysteresis, Berry-phase hysteresis, and spin structure: (a) experiment, (b) simulation, and (c) simulated spin structure in a field of -0.7 T. In (b), Q is the number of skyrmions per unit area (240 nm×240 nm×60 nm), and m is the normalized magnetization, M_z/M_s. The origin of the topological Hall effect due to spin texture—namely, the noncoplanar spin structure—is visible in (c).
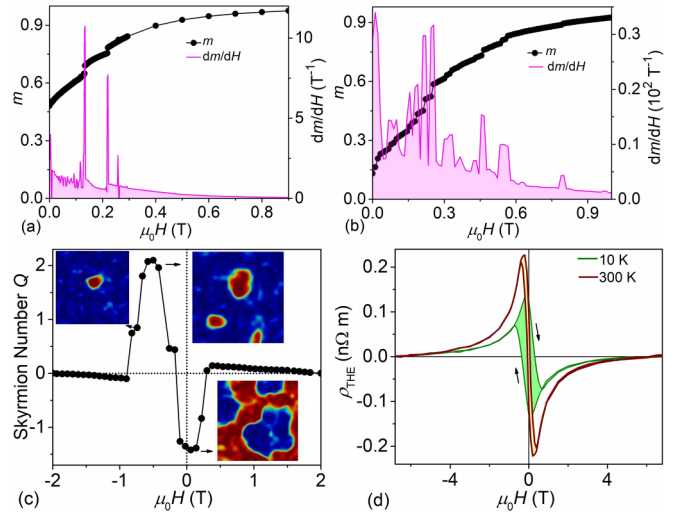

FIG. 3. Real structure and temperature effects: (a) experimental magnetization and susceptibility, (b) simulated magnetization and susceptibility, (c) the real-structure origin of the Berry-phase hysteresis, and (d) Berry-phase hysteresis at 10 K and 300 K. The susceptibility peaks in (a) and (b) reflect Barkhausen jumps and are strongly real-structure dependent.

Magnetization reversal in a thin film of nanoparticle magnets is strongly real-structure dependent, which affects the magnetic [12,50,51] and, especially, Berry-phase hysteresis loops. There is an intricate balance among an interatomic exchange, magnetocrystalline anisotropy, and magnetostatic interactions, which results in spin structures such as that in Fig. 2(c) at some specific magnetic field. While the real structure leads to loop deformation, it does not affect the key feature of Figs. 1(d)–1(i)—namely, red (or blue) regions in a blue (or red) background. This embedding is the origin of the THE. Note that the longitudinal resistivity of the cobalt nanoparticle thin film slightly increases with temperature, from 0.26 $\mu\Omega$ m at 10 K to 0.32 $\mu\Omega$ m at 300 K (Supplemental Material Fig. S7 [40]). This shows that the film is metallic and that the cobalt nanoparticles touch each other. This metallic contact is necessary to ensure exchange coupling between the nanoparticles and a noncollinear spin structure like that in Fig. 2(c).

Figures 3(a) and 3(b) illustrates the mathematical effect; by comparing the $M(H)$ curve (black) with its field derivative, the micromagnetic susceptibility $\chi = dM/dH$ (purple). While the experimental and theoretical $M(H)$ curves [Figs. 3(a) and 3(b), respectively] look similar, the derivative greatly enhances the differences. In the present system, the susceptibility peaks are due to Barkhausen jumps [50,52], which are strongly real-structure dependent. A schematic example of a Barkhausen jump is a fictitious transition from Figs. 1(d) to 1(f). These transition changes enhance the red area, and therefore the magnetization in a jump-like fashion. In fact, there are two types of Barkhausen jumps, which have not yet been distinguished in the literature. When the field changes the domain size and shape only, then Q remains constant,

but the Barkhausen-induced creation or merger of domains changes Q like the transition from Figs. 1(f) to 1(g).

Physically, the topological Hall signal critically depends on details of the magnetization process. Figure 3(c) outlines the situation in the present system by showing how the red and blue areas evolve in a magnetic field. In strongly negative fields, the magnetization is ↓ (blue) everywhere, but with increasing field, the magnetization starts to become noncoplanar noncollinear, and Eq. (1) yields a nonzero skyrmion density. The red regions grow and finally coalesce. This coalescence does not change the magnetization very much, but yields a drastic change in Q: red regions in a blue background become blue regions in a red background, which causes the sign of Q to switch. Since are investigating inhomogeneous nanoparticle thin film, the switching patterns exhibit considerable randomness [Fig. 3(c)], but this does not affect the overall topological picture.

The magnetization and magnetization reversal in the exchange-coupled cobalt nanoparticle film can be explained using the magnetization reversal process, as schematically shown in Supplemental Material Fig. S15 [40]. A key question is whether the reversal is noncooperative, as in Supplemental Material Figure S15(a) [40], compared to a cooperative reversal in Supplemental Material Figure S15(b) [40]. It is known that noncooperative reversal dominates in systems with broad switching-field distributions (small values of dM/dH), whereas narrow switching field distributions (large values of dM/dH) favor cooperative reversal [12]. The underlying physical mechanism is that the interatomic exchange proportional to A/R^2, where A is the exchange stiffness, competes against the anisotropy of strength K_1. For very small particles, as well as in very soft magnets (small K_1), the exchange dominates and the reversal is cooperative. Elemental cobalt is a prototypical semihard magnet and its particle size is fairly small, so we are in an intermediate regime closer

to cooperative reversal [Supplemental Material Fig. S15(b) [40]] than to noncooperative reversal [Supplement Material Fig. S15(a) [40]]. The sizes of the cooperative blocks are random, and some of the blocks are fairly large. The switching of such big blocks has the character of Barkhausen jumps.

Another intriguing aspect is an increase in the topological Hall effect with increasing temperature. As mentioned earlier, the cobalt nanoparticles are exchanged coupled, which exhibit cooperative magnetization reversal and subsequently gives rise to the chiral domains with chiral-domain walls, i.e., yellow boundary enclosing the region with uniform magnetization (Supplemental Material Fig. S1 [40]). As temperature increases, the exchange stiffness constant decreases in cobalt (see Supplemental Material [40] for the calculation of exchange stiffness in cobalt nanoparticles and Refs. [53–55] for more details). Second, at elevated temperatures, the reversal is not only accompanied by nucleation, but also by the thermal fluctuation of spins—i.e., the probability of flipping of spins increases as temperature increases because of a small increase in thermal energy (Ref. [55], Ch. 6). These two factors cause the magnetization reversal easier and lead to an increase in the number of individual domains with the noncoplanar spin structures. Therefore, an increase in temperature is expected to increase the intensity of the topological Hall effect as observed in the case of exchange-coupled cobalt nanoparticle film. This feature, linked to the high Curie temperature of cobalt, is an advantage because the noncoplanar spin texture with finite skyrmion number caused by B20 Dzyaloshinskii–Moriya interactions requires considerable effort at high temperatures [38]. It is worth noting that the chiral domains reported in this study are only quantified in terms of skyrmion numbers and are not traditional skyrmions caused by DMIs in B20-type materials and interfacial DMIs in multilayered thin films.

It is worth noting that anomalies in the Hall effect may also arise from two or multichannel Hall effects [56–58]. However, the two-channel Hall effect discussed in [56–58] can be ruled out in the exchange-coupled cobalt nanoparticle film. First, the two-channel Hall effect in the heterostructures discussed in Ref. [57] is solely due to the presence of the heavy-metal platinum layer, which causes the spin Hall effect, and also an anomalous Hall effect due to proximity-induced magnetization. These effects are not expected in homogeneous cobalt nanoparticle films. Second, inhomogeneous systems with the presence of a secondary magnetic phase often show bimodal switching field distributions in magnetization data [e.g., Fig. 4(d) in Refs. [56] and [59]] and subsequently yield the two-channel Hall effect. This bimodal two-channel effect generally arises in systems with combinations of hard and soft phases, which will not give narrow switching-field distribution, as discussed in Ref. [12]. In contrast, our cobalt nanoparticle film does not show any bimodal switching field distributions in the magnetization data [Fig. 2(a) and Supplemental Material Fig. S5 [40]]. Finally, in the case of manganese-doped Bi_2Se_3 discussed in Ref. [58], the two-channel Hall effect is caused by different magnetization contributions from bulk and surface, which is not the case in the exchange-coupled cobalt nanoparticle films. With all physical origins that cause the two-channel Hall effect [56–58] ruled out in the exchange-coupled cobalt nanoparticle

films, the anomalies observed in the Hall data are solely due to the topological Hall effect.

We also measured the change of magnetic domains of the cobalt nanoparticle film by MFM (see Fig. 4) and the corresponding AFM topography images at room temperature [40]. As discussed earlier, the exchange-coupled nanoparticles involve in cooperative magnetization reversal, and the reversed magnetic domains expand with increasing the magnetic field. This is seen from the phase images of MFM, which show that the individual magnetic domains with closed domain walls appear at around 0.04 T, and their size increases as the magnetic field increases. Our electron-transport data show that the THE has a maximum value in the region −0.02 T to 0.02 T. MFM images also shows a comparatively large number of smaller magnetic bubbles around this field region. Note that the bigger magnetic domains may still contain several small domains in the field region −0.02 T to 0.02 T, which could not be visualized due to the low resolution of MFM.

In the MFM images, the positive (negative) phase shift corresponds to the repulsive (attractive) force between the tip and magnetic stray field. When the sample is fully magnetized at a saturated field, the parallel alignment of the magnetic moment for the sample and tip should contribute to the negative phase. However, under lift mode, the severe change of surface roughness may perturb the phase signal, and there exist areas with a positive phase (the yellow region in the uneven surface) that persist even under 5 T. However, in a relatively flat area, the closed magnetic domains with negative phase signals undergo field-driven expanding and subsequent coalescence. Our AFM and MFM images (Fig. 4 and Supplemental Material Figs. S13 and S14 [40]) show that the region in which the field gradient disappear is almost even, while the region where the field gradient does not change has an uneven surface.

Magnetic hysteresis loops are typically plotted by showing the magnetization M as a function of the magnetic field H. Figures 2 and 3 show that this is also possible for Berry-phase hysteresis. However, such plots convolute magnetic and topological properties, because the field generally changes both $\boldsymbol{M}$ and its gradient $\nabla\boldsymbol{M}$. To remove this field effect, we introduce a new plot showing Q as a function of $m = M/M_s$ (Fig. 5). In this parametric $Q-M$ plot, each field corresponds to one point in $Q-M$ space, but this field is not shown explicitly unless each point of the curve is explicitly labeled by its field value.

The $Q-M$ plot provides not only an entirely new view of Berry-phase hysteresis, but also simplifies the analysis. In particular, $m = -1$ and $m = +1$ correspond to homogeneous magnetization states, so that $Q (m = \pm1) = 0$. Berry-phase hysteresis occurs for intermediate values of m, and Fig. 5(a) shows that this hysteresis is accompanied by a topological remanence Q_o. Approximating the $Q(m)$ by a cubic polynomial [61] yields

$$Q = (Q_o + Q_1 m)(1-m^2). \tag{3}$$

A cubic polynomial contains four parameters, but only two of them—namely, Q_o and the magnitude parameter Q_1—are adjustable. The remaining two parameters are implicitly fixed by the boundary conditions at $m = \pm1$. While Eq. (3) is a rather crude approximation, it works surprisingly well for the present system, as evidenced by the comparison with the experiment in Fig. 5(b).
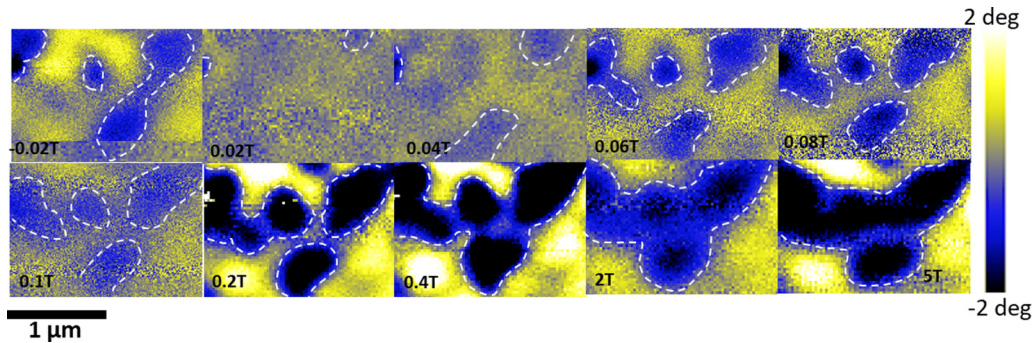
FIG. 4. MFM image and magnetization reversal: MFM image of magnetization reversal in a region with an even surface (blue region). The magnetization reversal starts randomly making domains at a field of 0.06 T, and these domains expand as the field is increased, and finally, coalescence of the domain occurs at a high field. Note that not only do we have topological Hall effect contributions due to magnetic domains, but also we have topological Hall effect contributions due to chiral spin inhomogeneity, and imaging of these chiral spins texture is difficult [47,60].

Figures 5(c)–5(g) shows how the Berry-phase hysteresis evolves in a simple, exactly solvable model. Circular red domains are arranged on a triangular lattice [Fig. 5(c)] and grow in the external field [Fig. 5(c)]. At the phase transition point, the domains t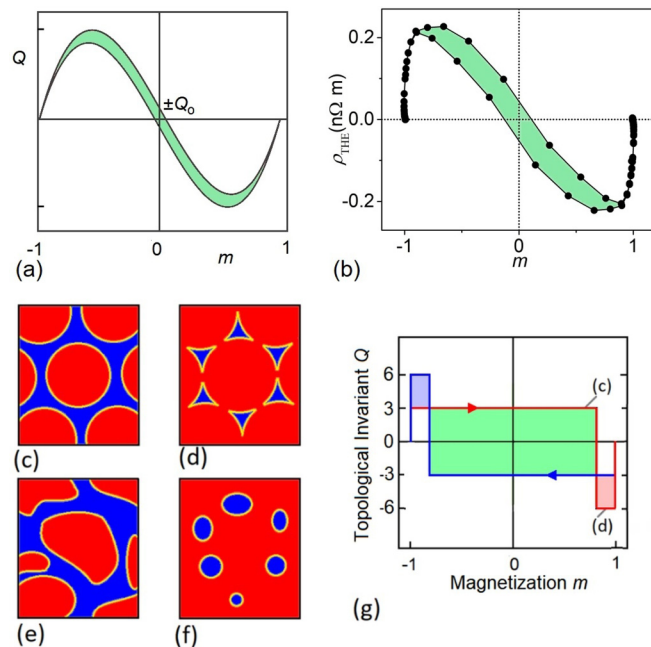ouch and start to overlap, so that the back-ground changes from blue to red and the THE changes sign. Figure 5(g) shows the $Q-M$ plot for the model of Figs. 5(c) and 5(d). The transition is triggered by an external magnetic field, but near the transition point there is only a trivially small magnetization change. We also note that the transition [Figs. 5(c) and 5(d)] occurs at a point where most of the area is red (↑) already, at a magnetization of $\pi/\sqrt{3}-1 \approx 0.814\, M_s$. This is the reason for the striking width of the green topological hysteresis loop in Fig. 5(g).

The light-blue and light-red areas in Fig. 5(g) are model specific and are related to the duality of the assumed skyrmion lattice. Figures 5(c) and 5(d) corresponds to triangular and honeycomb lattices, respectively, which are dual but have different numbers of sites per honeycomb unit cell (three and six). By comparison, square lattices are self-dual, which causes the bright areas to disappear. In the light of this model analysis, the difference between the red/blue curves in Figs. 2(a) and 2(b) is not surprising, but a comprehensive explanation of the duality effect is a challenge to future mathematical and physical research. The domain structures with domain-wall chirality of Figs. 5(e) and 5(f) are topologically but not micromagnetically equivalent to Figs. 5(c) and 5(d), and yield a real–structure-dependent smoothing of the rectangular loop parts in Fig. 5(g).

It is interesting to note that domain structures like those in Figs. 1 and 5 have been around for decades [50,62], as it has the recognition of features such as domain-wall chirality [62,63]. However, at that time, neither the Berry phase nor the topological Hall effect was widely aware [5,32,37]. Furthermore, the initial research focused on bubble domains of fairly large sizes L, typically micron size. Each reverse domain contributes one flux quantum to the THE, so that the net effect scales a $1/L^2$. Even today, such small effects are nontrivial to detect without the help of DMIs [17], and this is the main reason for our consideration of cobalt nanoparticle thin films, where L is a few 10 nm.

Future applications of Berry-phase hysteresis in spin electronics and beyond [64–66] are difficult to judge. The low skyrmion mobility in the present nanoparticle system will probably prevent applications such as racetrack memories [64], but three arguments speak in favor of the potential technological usefulness of Berry-phase hysteresis. First, the small feature size addresses miniaturization requirements

FIG. 5. Analytical modeling of Berry-phase hysteresis: (a) most general cubic plot of skyrmion number Q as a function of magnetization, (b) experimental $Q-M$ plot, (c) and (d) topological phase transition in a simple circular-domain model, (e) and (f) topologically equivalent version of the same model, and (g) Berry-phase hysteresis loop for the model of (c) and (d). The transitions from (c) to (d) and from (e) to (f) are triggered by a magnetic field increase and are accompanied by an incremental magnetization increase only. In (g), the transition occurs at a fairly high value of $M_z = \pm 0.814\, M_s$. At $M_z = \pm M_s$, Q jumps to zero, because the residual domains are annihilated at saturation. The light-blue and light-red areas in (g) are a duality effect caused by the triangular skyrmion lattice assumed in (a) and (b). As in other parts of this work, m is the normalized magnetization ($m = M_z/M_s$).

in spin electronics. Second, cobalt has a very high Curie temperature, which facilitates the measurement and practical exploitation of its THE. In fact, Fig. 3(d) shows that the effect actually *increases* with temperature. By contrast, noncentrosymmetric materials tend to have rather low magnetic ordering temperatures, requiring considerable effort to drive the systems beyond room temperature [23,38]. Third, the effect has a very high field sensitivity, as one can see from Fig. 3(d), and by comparing the maximum slopes of the red, blue, and black curves in Fig. 2(b).

IV. CONCLUSION

The starting point and first main finding in this work is the recognition that thin-film magnetization reversal has the character of a topological phase transition. The transition is accompanied by Berry-phase hysteresis, a phenomenon very different from ordinary magnetic hysteresis and exhibiting features such as topological remanence and micromagnetic duality. The new concept has led to the development of a topology-specific plot showing the skyrmion number as a function of magnetization rather than the field. In our cobalt nanoparticle system, Berry-phase hysteresis is realized on a nanoscale, increases with temperature, and exhibits a high field sensitivity. Several interdisciplinary challenges emerge from the present work. For example, it is intriguing to see which other systems investigated in the past, present, and future exhibit Berry-phase hysteresis and how it is realized.

[1] J. M. Kosterlitz, Rev. Mod. Phys. **89**, 040501 (2017).

[2] Ch. Lin *et al.*, Nat. Mater. **20**, 1093 (2021).

[3] M. Levin and X.-G. Wen, Phys. Rev. Lett. **96**, 110405 (2006).

[4] X.-G. Wen, *Quantum-Field Theory of Many-Body Systems* (Oxford University Press, Oxford, 2004).

[5] D. Xiao, M.-Ch. Chang, and Q. Niu, Rev. Mod. Phys. **82**, 1959 (2010).

[6] B. A. Bernevig, T. L. Hughes, and S.-C. Zhang, Science **314**, 1757 (2006).

[7] I. M. Lifshitz, Sov. Phys. J. Exptl. Theoret. Phys. **11**, 1130 (1960).

[8] J. M. Kosterlitz and D. J. Thouless, J. Phys. C **6**, 1181 (1973).

[9] H. Huang and F. Liu, Research **2020**, 7832610 (2020).

[10] E. Warburg, Ann. Phys. (Leipzig) **249**, 141 (1881).

[11] M. Dörries, Hist. Stud. Nat. Sci. **22**, 25 (1991).

[12] R. Skomski, J. Phys.: Condens. Matter **15**, R841 (2003).

[13] L. D. Barron, in *Chirality at the Nanoscale*, edited by D. B. Amabilino (Wiley, New York, 2009), pp. 1–27.

[14] W. Jiang, P. Upadhyaya, W. Zhang, G. Yu, M. B. Jungfleisch, F. Y. Fradin, J. E. Pearson, Y. Tserkovnyak, K. L. Wang, O. Heinonen, S. G. E. te Velthuis, and A. Hoffmann, Science **349**, 283 (2015).

[15] M. Lonsky and A. Hoffmann, Phys. Rev. B **102**, 104403 (2020).

[16] S.-G. Je, H.-S. Han, S. K. Kim, S. A. Montoya, W. Chao, I.-S. Hong, E. E. Fullerton, K.-S. Lee, K.-J. Lee, M.-Y. Im, and J.-I. Hong, ACS Nano **14**, 3251 (2020).

[17] W. Zhang, B. Balasubramanian, A. Ullah, R. Pahari, X. Li, L. Yue, S. R. Valloppilly, A. Sokolov, R. Skomski, and D. J. Sellmyer, Appl. Phys. Lett. **115**, 172404 (2019).

[18] W. Wang, Y.-F. Zhao, F. Wang, M. W. Daniels, C.-Z. Chang, J. Zang, D. Xiao, and W. Wu, Nano Lett. **21**, 1108 (2021).

[19] P. Li, J. Ding, S. S.-L. Zhang, J. Kally, T. Pillsbury, O. G. Heinonen, G. Rimal, Ch. Bi, A. DeMann, S. B. Field, W. Wang, J. Tang, J. S. Jiang, A. Hoffmann, N. Samarth, and M. Wu, Nano Lett. **21**, 84 (2021).

[20] E. Y. Vedmedenko, R. K. Kawakami, D. D. Sheka, P. Gambardella, A. Kirilyuk, A. Hirohata, C. Binek, O. Chubykalo-Fesenko, S. Sanvito, J. Grollier, K. Everschor-Sitte, T. Kampfrath, C.-Y. You, and A. Berger, J. Phys. D Appl. Phys. **53**, 453001 (2020).

[21] Y. Taguchi, Y. Oohara, H. Yoshizawa, N. Nagaosa, and Y. Tokura, Science **291**, 2573 (2001).

[22] M. Z. Hasan and C. L. Kane, Rev. Mod. Phys. **82**, 3045 (2010).

[23] Y. Tokunaga, X. Yu, J. White, H. M. Rønnow, D. Morikawa, Y. Taguchi, and Y. Tokura, Nat. Commun. **6**, 7638 (2015).

[24] K. G. Rana, O. Meshcheriakova, J. Kübler, B. Ernst, J. Karel, R. Hillebrand, E. Pippel, P. Werner, A. K. Nayak, C. Felser, and S. S. P. Parkin, New J. Phys. **18**, 085007 (2016).

[25] A. Soumyanarayanan, N. Reyren, A. Fert, and C. Panagopoulos, Nature (London) **539**, 509 (2016).

[26] D. S. Sanchez *et al.*,, Nature (London) **567**, 500 (2019).

[27] M. Raju, A. Yagil, A. Soumyanarayanan, A. K. C. Tan, A. Almoalem, Fusheng Ma, O. M. Auslaender, and C. Panagopoulos, Nat. Commun. **10**, 696 (2019).

[28] A. K. Sharma, J. Jena, K. G. Rana, A. Markou, H. L. Meyerheim, K. Mohseni, A. K. Srivastava, I. Kostanoskiy, C. Felser, and S. S. P. Parkin, Adv. Mater. **33**, 2101323 (2021).

[29] M. Tomé and H. D. Rosales, Phys. Rev. B **103**, L020403 (2021).

[30] J. P. Pekola, K. Torizuka, A. J. Manninen, J. M. Kyynäräinen, and G. E. Volovik, Phys. Rev. Lett. **65**, 3293 (1990).

[31] N. Nagaosa and Y. Tokura, Nat. Nanotechnol. **8**, 899 (2013).

[32] A. Neubauer, C. Pfleiderer, B. Binz, A. Rosch, R. Ritz, P. G. Niklowitz, and P. Böni, Phys. Rev. Lett. **102**, 186602 (2009).

[33] S. Seki and M. Mochizuki, *Skyrmions in Magnetic Materials* (Springer International, Cham, 2016).

[34] Y. Fujishiro, N. Kanazawa, T. Nakajima, X. Z. Yu, K. Ohishi, Y. Kawamura, K. Kakurai, T. Arima, H. Mitamura, A. Miyake, K. Akiba, M. Tokunaga, A. Matsuo, K. Kindo, T. Koretsune, R. Arita, and Y. Tokura, Nat. Commun. **10**, 1059 (2019).

[35] L. Pierobon, C. Moutafis, Y. Li, and J. F. Löffler, Sci. Rep. **8**, 16675 (2018).

[36] S. Das *et al.*, Nat. Mater. **20**, 194 (2021).

[37] M. V. Berry, Proc. R. Soc. London A **392**, 45 (1984).

[38] B. Balasubramanian, P. Manchanda, R. Pahari, Z. Chen, W. Zhang, S. R. Valloppilly, X. Li, A. Sarella, L. Yue, A. Ullah, P. Dev, D. A. Muller, R. Skomski, G. C. Hadjipanayis, and D. J. Sellmyer, Phys. Rev. Lett. **124**, 057201 (2020).

[39] R. Skomski, B. Balasubramanian, A. Ullah, C. Binek, and D. J. Sellmyer, AIP Adv. **12**, 035341 (2022).

[40] See Supplemental Material at http://link.aps.org/supplemental/10.1103/PhysRevB.106.134430 for additional details on methods and additional results, which also include Refs. [67–71].

[41] W. Fenchel, Math. Ann. **101**, 238 (1929).

[42] Y. He, T. Helm, I. Soldatov, S. Schneider, D. Pohl, A. K. Srivastava, A. K. Sharma, J. Kroder, W. Schnelle, R. Schaefer, B. Rellinghaus, G. H. Fecher, S. S. P. Parkin, and C. Felser, Phys. Rev. B **105**, 064426 (2022).

[43] H. Seifert, Acta Math. **60**, 147 (1933).

[44] J. W. Zwanziger, M. Koenig, and A. Pines, Annu. Rev. Phys. Chem. **41**, 601 (1990).

[45] B. Ding, J. Zhang, H. Li, S. Zhang, E. Liu, G. Wu, X. Zhang, and W. Wang, Appl. Phys. Lett. **116**, 132402 (2020).

[46] B. Balasubramanian, T. A. George, P. Manchanda, R. Pahari, A. Ullah, R. Skomski, and D. J. Sellmyer, Phys. Rev. Mater. **5**, 024402 (2021).

[47] R. Pahari, B. Balasubramanian, A. Ullah, P. Manchanda, H. Komuro, R. Streubel, C. Klewe, Shah R. Valloppilly, P. Shafer, P. Dev, R. Skomski, and D. J. Sellmyer, Phys. Rev. Mater. **5**, 124418 (2021).

[48] M. Beg, M. Lang, and H. Fangohr, IEEE Trans. Magn. **58**, 7300205 (2022).

[49] (our code is publicly available at https://github.com/ubermag/help/issues/110#issuecomment-970591821)

[50] A. Hubert and R. Schäfer, *Magnetic Domains* (Springer-Verlag, Berlin, 1998).

[51] L. Exl, D. Suess, and T. Schrefl, in *Handbook of Magnetism and Magnetic Materials*, edited by J. M. D. Coey and S. S. Parkin (Springer, Cham, 2021), pp. 347–390.

[52] H. Barkhausen, Phys. Z. **20**, 401 (1919).

[53] H. Kronmüller and M. Fähnle, *Micromagnetism and the Microstructure of Ferromagnetic Solids* (Cambridge University Press, Cambridge, 2003).

[54] R. Moreno, R. F. L. Evans, S. Khmelevskyi, M. C. Munoz, R. W. Chantrell, and O. Chubykalo-Fesenko, Phys. Rev. B **94**, 104433 (2016).

[55] J. M. D. Coey, *Magnetism and Magnetic Materials* (Cambridge University Press, New York, 2010).

[56] G. Kimbell, P. M. Sass, B. Woltjes, E. K. Ko, T. W. Noh, W. Wu, and J. W. A. Robinson, Phys. Rev. Mater. **4**, 054414 (2020).

[57] A. Gerber, Phys. Rev. B **98**, 214440 (2018).

[58] S. Ding, Z. Liang, C. Yun, R. Wu, M. Xue, Z. Lin, A. Ross, S. Becker, W. Yang, X. Ma, D. Chen, K. Sun, G. Jakob, M. Kläui, and J. Yang, Phys. Rev. B **104**, 224410 (2021).

[59] N. Liu, J. Teng, and Y. Li, Nat. Commun. **9**, 1282 (2018).

[60] H. Wang, B. Balasubramanian, R. Pahari, R. Skomski, Y. Liu, A. Huq, D. J. Sellmyer, and X. Xu, Phys. Rev. Mater. **3**, 064403 (2019).

[61] W. Zhang, B. Balasubramanian, Y. Sun, A. Ullah, R. Skomski, R. Pahari, S. R. Valloppilly, X.-Zh. Li, C.-Zh. Wang, K.-M. Ho, and D. J. Sellmyer, J. Magn. Magn. Mater. **537**, 168104 (2021).

[62] P. J. Grundy and S. R. Herd, Phys. Status Solidi (A) **20**, 295 (1973).

[63] J. Jiang, D. Xiao, F. Wang, J.-H. Shin, D. Andreoli, J. Zhang, R. Xiao, Y.-F. Zhao, M. Kayyalha, L. Zhang, K. Wang, J. Zang, C. Liu, N. Samarth, M. H. W. Chan, and C.-Z. Chang, Nat. Mater. **19**, 732 (2020).

[64] S. S. P. Parkin, M. Hayashi, and L. Thomas, Science **320**, 190 (2008).

[65] A. Fert, N. Reyren, and V. Cros, Nat. Rev. Mater. **2**, 17031 (2017).

[66] C. Back, V. Cros, H. Ebert, K. Everschor-Sitte, A. Fert, M. Garst, T. Ma, S. Mankovsky, T. L. Monchesky, M. Mostovoy, N. Nagaosa, and S. S. P. Parkin, J. Phys. D **53**, 363001 (2020).

[67] A. A. Thiele, Bell Syst. Tech. J. **48**, 3287 (1969).

[68] W. Koshibae and N. Nagaosa, New J. Phys. **18**, 045007 (2016).

[69] B. Balasubramanian, X. Zhao, S. R. Valloppilly, S. Beniwal, R. Skomski, A. Sarella, Y. Jin, X. Li, X. Xu, H. Cao, H. Wang, A. Enders, C.-Z. Wang, K.-M. Ho, and D. J. Sellmyer, Nanoscale **10**, 13011 (2018).

[70] X. H. Zhang, T. R. Gao, L. Fang, S. Fackler, J. A. Borchers, B. J. Kirby, B. B. Maranville, S. E. Lofland, A. T. N'Diaye, E. Arenholz, A. Ullah, J. Cui, R. Skomski, and I. Takeuchi, J. Magn. Magn. Mater. **560**, 169627 (2022).

[71] R. Skomski and J. M. D. Coey, *Permanent Magnetism* (Institute of Physics, Bristol, 1999).